PROCEEDINGS OF SPIE

SPIEDigitalLibrary.org/conference-proceedings-of-spie

# Crack-tip deformation field measurements using coherent gradient sensing

Hareesh V. Tippur, Sridhar Krishnaswamy, Ares J. Rosakis

Hareesh V. Tippur, Sridhar Krishnaswamy, Ares J. Rosakis, "Crack-tip deformation field measurements using coherent gradient sensing," Proc. SPIE 1554, Second International Conference on Photomechanics and Speckle Metrology, (1 December 1991); doi: 10.1117/12.49513

SPIE.

Event: San Diego, '91, 1991, San Diego, CA, United States

# Crack Tip Deformation Field Measurements Using Coherent Gradient Sensing

Hareesh V. Tippur[1], Sridhar Krishnaswamy[2] and Ares J. Rosakis[3]

## Abstract

A real time, full field, lateral shearing interferometry - *coherent gradient sensing* (CGS) - has recently been developed for investigating fracture in transparent and opaque solids. The resulting interference patterns are related to the mechanical fields by means of a first order diffraction analysis. The method has been successfully applied to quasi-static and dynamic crack tip deformation field mapping in homogeneous and bimaterial fracture specimens.

## Introduction

In recent times, optical methods have greatly assisted in understanding the fracture mechanics of solids through local crack tip field measurements [1]. Photoelasticity [2], geometric moire methods [3,4], and caustics [5,6] are some of the commonly used incoherent optical methods in fracture mechanics. Moire interferometry [7], holography [8], Twyman-Green interferometry [9] fall into the category of coherent optical methods used in experimental fracture mechanics. These techniques can be readily applied to quasi-static, elastic and/or elasto-plastic crack growth investigations. For measuring crack tip fields near dynamically growing cracks, however, photoelasticity [10,11] and caustics [12] are generally used. Optically birefringent models are required for dynamic photoelastic studies while the method of caustics can be used with both opaque and transparent solids. Caustics, however, is not a full field optical method and hence finer details of the crack tip fields may not be apparent. There has been a need for a simple, full field technique for dynamic fracture mechanics which can be used with either opaque solids or optically isotropic transparent solids.

A relatively new optical method, *coherent gradient sensing* (CGS) has been developed for quasi-static and dynamic fracture mechanics investigations. It is a lateral shearing interferometry wherein a pair of gratings is used as a wave front shearing device. CGS has several advantages. It provides full field interference patterns corresponding to the deformation fields in real time. The method can be applied to crack tip field measurements in both transmission mode and reflection mode. This feature allows one to use CGS to study either optically isotropic transparent solids or opaque solids. The relative insensitivity to vibrations, controllability of resolution of measurements and simplicity are some of the additional advantages. The purpose of this article is to present a review of the method and provide examples which demonstrate the feasibility and applicability of CGS to the study of quasi-static and dynamic fracture of homogeneous and bimaterial solids.

## Coherent Gradient Sensing

*Experimental Set-up*

In Fig.(1) the schematic of the experimental set up used for transmission CGS is shown. A transparent, optically isotropic specimen is illuminated by a collimated bundle of laser light. The transmitted object wave is then incident on a pair of chromium-on-glass master gratings, $G_1$ and $G_2$, separated by a distance $\Delta$. The field distribution on the $G_2$ plane is gathered by a lens $L_1$ and its spatial frequency content is

[1]Auburn University, Auburn, AL
[2]Northwestern University, Evanston, IL
[3]California Institute of Technology, Pasadena, CA

displayed on its back focal plane. Information around either the $\pm 1$ diffraction orders is filtered in order to obtain interference patterns representing stress gradients on the image plane.

Figure (2) shows the modification of the above set up for measuring surface deflections of opaque solids when studied in reflection mode. In this case, the specularly reflecting object surface is illuminated by a collimated beam of laser light using a beam splitter. The reflected beam, as in the previous case, gets processed through the optical arrangement which is identical to the one shown in Fig.(1).

A first order diffraction analysis is presented in the next sections will demonstrate that the interference patterns obtained are related to local crack tip deformations namely, gradients of in-plane stress or gradients of out-of-plane displacement.

*Working Principle*

The process of object wave shearing by a pair of line gratings is shown schematically in Fig.(3). For the sake of simplicity of representation, the line gratings are assumed to have a *sinusoidal transmittance.* Let the grating lines of $G_1$ and $G_2$ be parallel to, say, the $x_1$-axis. A plane wave transmitted through or reflected from an undeformed specimen and propagating along the optical axis, is diffracted into three plane wave fronts $E_0, E_1$ and $E_{-1}$ by the first grating $G_1$. The magnitude of the angle between the propagation directions of $E_0$ and $E_{\pm 1}$ is given by the diffraction equation $\theta = \sin^{-1}(\lambda/p)$, where $\lambda$ is the wave length and $p$ is the grating pitch. Upon incidence on the second grating $G_2$, the wave fronts are further diffracted into $E_{(0,0)}$, $E_{(0,1)}$, $E_{(1,-1)}$, $E_{(1,0)}$, $E_{(1,1)}$ etc. These wave fronts which are propagating in distinctly different directions, are then brought to focus at spatially separated diffraction spots on the back focal plane of the filtering lens. The spacing between these diffraction spots is directly proportional to $\sin\theta$ or inversely proportional to the grating pitch $p$.

Now, consider a plane wave normally incident on a deformed specimen surface. The resulting transmitted or reflected wave front will be distorted either due to changes of refractive index or due to surface deformations. This object wave front that is incident on $G_1$ now carries information regarding the specimen deformation, and consists of light rays travelling with small perturbations to their initial direction parallel to the optical axis. If a large portion of such a bundle of light has rays nearly parallel to the optical axis, each of the diffraction spots on the focal plane of $L_1$ will be locally surrounded by a halo of dispersed light field due to the deflected rays. The extent of this depends on the magnitude of the deformations. By using a planar aperture at the filtering plane, information existing around one of the spots can be further imaged.

*Analysis*

Consider a specimen whose midplane, in transmission, or surface, in reflection, occupies the $(x_1, x_2)$ plane in the undeformed state. Let $\mathbf{e_i}$ denote unit vector along $x_i$-axis, $(i = 1, 2, 3)$ [see Fig.(4)]. When the specimen is undeformed, the unit object wave propagation vector $\mathbf{d_0} = \mathbf{e_3}$. After deformation, the propagation vector is perturbed and can be expressed by,

$$\mathbf{d_0} = \alpha_o \mathbf{e_1} + \beta_o \mathbf{e_2} + \gamma_o \mathbf{e_3}, \tag{1}$$

where $\alpha_o(x_1, x_2)$, $\beta_o(x_1, x_2)$, and $\gamma_o(x_1, x_2)$ denote the direction cosines of the perturbed wave front. This upon incidence on $G_1$, the grating lines of which are parallel to, say, the $x_1$-axis, is split into three wave fronts propagating along $\mathbf{d_0}$, $\mathbf{d_{\pm 1}}$ and whose amplitudes $E_0(\mathbf{x}')$, $E_{\pm 1}(\mathbf{x}')$ can be represented by,

$$E_0(\mathbf{x}') = a_0 \exp[ik\mathbf{d_0} \cdot \mathbf{x}'], \qquad E_{\pm 1}(\mathbf{x}') = a_{\pm 1} \exp[ik\mathbf{d_{\pm 1}} \cdot \mathbf{x}'], \tag{2}$$

where $a_0$ and $a_{\pm 1}$ are constants and $k = 2\pi/\lambda$ is the wave number. Now, the propagation directions of the diffracted wave fronts can be related to the direction cosines of the incident propagation vector through [See Ref.13 for details],

$$\mathbf{d_{\pm 1}} = [\alpha_o \mathbf{e_1} + (\beta_o \cos\theta \pm \gamma_o \sin\theta)\mathbf{e_2} + (\gamma_o \cos\theta \mp \beta_o \sin\theta)\mathbf{e_3}], \tag{3}$$

using the diffraction equation $\theta = \sin^{-1}(\lambda/p)$. On the plane $G_2$ ($x_3' = \Delta$) [see Fig.(4)], the amplitude distribution of the three diffracted wave fronts are,

$$E_0|_{x_3'=\Delta} = a_0 \exp\left[ik\left(\frac{\Delta}{\gamma_o}\right)\right], \tag{4}$$

$$E_{\pm 1}|_{x_3'=\Delta} = a_1 \exp\left[ik\frac{\Delta}{(\gamma_o \cos\theta \mp \beta_o \sin\theta)}\right]. \tag{5}$$

The wave fronts $E_0$, $E_{\pm 1}$ will undergo further diffraction upon incidence on $G_2$ into secondary wave fronts $E_{(0,0)}$, $E_{(0,1)}$, $E_{(1,-1)}$, $E_{(1,0)}$, $E_{(1,1)}$ etc. Of these secondary diffractions, $E_{(0,1)}$ and $E_{(1,0)}$ have their propagation direction along $\mathbf{d_1}$, $E_{(0,-1)}$ and $E_{(-1,0)}$ along $\mathbf{d_{-1}}$ and $E_{(0,0)}$, $E_{(-1,1)}$ and $E_{(1,-1)}$ along $\mathbf{d_0}$ [Fig.(3)]. If the information is spatially filtered by blocking all but $\pm 1$ diffraction order, only the wave fronts $E_{(0,\pm 1)}$ and $E_{(\pm 1,0)}$ contribute to the formation of the image. Noting that the two wave fronts do not acquire any additional relative phase differences after $G_2$, the amplitude distribution on the image plane is,

$$E_{im} = (E_0 + E_{\pm 1})|_{x_3'=\Delta} = a_0 \exp\left[ik\left(\frac{\Delta}{\gamma_o}\right)\right] + a_{\pm 1} \exp\left[ik\frac{\Delta}{(\gamma_o \cos\theta \mp \beta_o \sin\theta)}\right]. \tag{6}$$

Hence, the intensity distribution on the image plane, for small $\theta$ and small deflections ($\gamma \approx 1$), is,

$$I_{im} = E_{im}E_{im}^* = a_0^2 + a_{\pm 1}^2 + 2a_0 a_{\pm 1} \cos(k\Delta\beta_o\theta), \tag{7}$$

where $E_{im}^*$ is the complex conjugate of $E_{im}$. Thus, $I_{im}$ denotes an intensity variation on the image plane whose maxima occur when

$$k\Delta\beta_o\theta = 2M_2\pi, \qquad M_2 = 0, \pm 1, \pm 2, ...., \tag{8}$$

where $M_2$ denotes fringe orders. Similarly, when the grating lines of $G_1$ and $G_2$ are parallel to the $x_2$-axis, it can be shown that,

$$k\Delta\alpha_o\theta = 2M_1\pi, \qquad M_1 = 0, \pm 1, \pm 2, .... \tag{9}$$

Equations (8) and (9) are the governing equations for the method of CGS and they relate fringe orders to the direction cosines of the object wave front. In the above two equations note that the sensitivity of measurement can be easily controlled by either the grating separation distance $\Delta$ or the grating pitch $p$.

*Direction Cosines and Crack Tip Deformations*

The direction cosines of the object wave front can be related to crack tip deformations for both transmission and reflection CGS.

*(a) Transmission*

Consider a planar wave front normally incident on an optically isotropic, transparent plate of uniform nominal thickness $h$ and refractive index $n_0$. Now, if the plate is deformed, the transmitted wave front acquires an optical path change $\delta S$ which is given by the elasto-optical equation [14],

$$\delta S(x_1, x_2) = 2h(n_0 - 1)\int_0^{1/2} \epsilon_{33}\, d(x_3/h) + 2h\int_0^{1/2} \delta n_0\, d(x_3/h). \tag{10}$$

The first term represents the net optical path difference due to the plate thickness change caused by the strain component $\epsilon_{33}$. The second term is due to the stress induced change in refractive index of the material. This change in the refractive index $\delta n_0$ is given by the Maxwell relation,

$$\delta n_0(x_1, x_2) = D_1(\sigma_{11} + \sigma_{22} + \sigma_{33}),$$

where $D_1$ is the stress-optic constant and $\sigma_{ij}$ are stress components. For an isotropic, linear elastic solid, strain component $\epsilon_{33}$ can be related to stresses and thus Eqn.(10) can be written as,

$$\delta S = 2h\left(D_1 - \frac{\nu}{E}(n_0 - 1)\right)\int_0^{1/2}\left\{(\sigma_{11}+\sigma_{22})\ \left[1 + D_2\ \left(\frac{\sigma_{33}}{\nu(\sigma_{11}+\sigma_{22})}\right)\right]\right\} d(x_3/h), \tag{11}$$

where $D_2 = \frac{\nu D_1 + \frac{\nu(n_0-1)}{E}}{D_1 - \frac{\nu(n_0-1)}{E}}$, $E$ and $\nu$ are the Young's modulus and the Poisson's ratio of the material, respectively. The above equation is written in such a way that the second term in the square brackets represents the degree of plane strain. When plane stress is a good approximation, this term can be neglected and Eqn.(11) reduces to,

$$\delta S \approx ch(\hat{\sigma}_{11} + \hat{\sigma}_{22}), \tag{12}$$

where $c = D_1 - \frac{\nu}{E}(n_0 - 1)$ and $\hat{\sigma}_{11}$ and $\hat{\sigma}_{22}$ are thickness averages of stress components of the material. Using these, the propagation vector for a perturbed wave front can be expressed as,

$$\mathbf{d_0} = \frac{\nabla(S)}{|\nabla(S)|} \approx \frac{\partial(\delta S)}{\partial x_1}\mathbf{e_1} + \frac{\partial(\delta S)}{\partial x_2}\mathbf{e_2} + \mathbf{e_3} \tag{13}$$

for $|\nabla(\delta S)|^2 << 1$ and where $S(x_1, x_2, x_3) = x_3 + \delta S(x_1, x_2)$=constant. Using Eqn.(13) in Eqn.(1), we can obtain the direction cosines of the propagation vector. Also, by comparing Eqn.(13) with Eqns. (8) and (9), the fringes can be related to the gradients of $(\hat{\sigma}_{11} + \hat{\sigma}_{22})$ as follows:

$$ch\frac{\partial(\hat{\sigma}_{11} + \hat{\sigma}_{22})}{\partial x_\alpha} \approx \frac{M_\alpha p}{\Delta}, \qquad M_\alpha = 0, \pm 1, \pm 2..., \qquad \alpha = 1, 2. \tag{14}$$

*(b) Reflection*

Consider a specimen whose reflective surface occupies the $(x_1, x_2)$ plane in the undeformed state [Fig.(4)]. Upon deformation, the reflector can be expressed as,

$$F(x_1, x_2, x_3) = x_3 + u_3(x_1, x_2) = 0. \tag{15}$$

where $u_3$ is the out-of-plane displacement component. The unit surface normal $\mathbf{N}$ at a generic point $O(x_1, x_2)$ is given by,

$$\mathbf{N} = \frac{\nabla F}{|\nabla F|} \approx u_{3,1}\mathbf{e_1} + u_{3,2}\mathbf{e_2} + \mathbf{e_3} \tag{16}$$

$u_{3,\alpha}$ implies differentiation with respect to $x_\alpha$. Consider now, a plane wave which is incident on the specimen along the $-x_3$ direction. Let $\mathbf{d_0}$ be the unit vector along the reflected ray whose direction cosines are $\alpha_o$, $\beta_o$ and $\gamma_o$. From the law of reflection, and noting that vectors $\mathbf{d_0}$, $\mathbf{N}$ and $\mathbf{e_3}$ are coplanar, one can show that [13] the direction cosines of $\mathbf{d_0}$ can be related to the gradients of $u_3$ by,

$$\alpha_o \approx 2u_{3,1}, \qquad \beta_o \approx 2u_{3,2}, \qquad \gamma_o \approx 1. \tag{17}$$

Using the above in Eqns. (8) and (9), we get,

$$\frac{\partial u_3}{\partial x_\alpha} \approx \frac{M_\alpha p}{2\Delta}, \qquad M_\alpha = 0, \pm 1, \pm 2, .... \tag{18}$$

where the fact that $\theta \approx (\lambda/p)$ and $k = 2\pi/\lambda$ are made use of. For an isotropic, linear elastic solid, out-of-plane displacement $u_3$ can be expressed as follows:

$$u_3 = -\frac{\nu h}{E}\int_0^{1/2}\left\{(\sigma_{11}+\sigma_{22})\left[1 - \frac{\sigma_{33}}{\nu(\sigma_{11}+\sigma_{22})}\right]\right\} d(x_3/h). \tag{19}$$

In the above, the second term in the square brackets represents the degree of plane strain and when plane stress is a good approximation, it can be neglected. Thus, the above equation reduces to,

$$u_3 = -\frac{\nu h}{2E}(\hat{\sigma}_{11} + \hat{\sigma}_{22}). \tag{20}$$

Hence Eqns. (18) can be expressed as,

$$\frac{\partial u_3}{\partial x_\alpha} = -\frac{\nu h}{2E}\frac{\partial(\hat{\sigma}_{11} + \hat{\sigma}_{22})}{\partial x_\alpha} = \left(\frac{M_\alpha p}{2\Delta}\right) \qquad M_\alpha = 0, \pm 1, \pm 2, .... \tag{21}$$

## Applications to Fracture Mechanics

*(a) Static Experiments*

Fracture specimens for *transmission* CGS are made from a sheet of PMMA of nominal thickness 9 mm. The specimen geometry and the three point bend loading configuration used is shown in Fig.(5). Several different crack length ($a$) to plate width ($w$) ratios, are studied. A band saw, approximately 0.75 mm thick, is used to cut notches in these specimen. A collimated laser beam of diameter 50 mm is centered around the crack tip and transmitted through the specimens in these experiments. The object wave front propagates through a pair of line gratings of density 40 lines per mm with a separation distance $\Delta$=30 mm. For the experimental parameters chosen, the sensitivity of measurement is approximately 0.025 degree/fringe. Figure (6) shows the crack tip fringes ($a/w = 0.2$) when the grating lines are perpendicular to the $x_1$- and $x_2$-axes, respectively, for an applied load $P$=1775 N. These fringes represent contour maps of constant $ch\frac{\partial(\hat{\sigma}_{11}+\hat{\sigma}_{22})}{\partial x_\alpha}$, [see, Eqn.(14)].

For analyzing the crack tip deformation fringes, a linear elastic plane stress asymptotic field is assumed to prevail in the crack tip vicinity. Using Williams' expansion [15] for mode-I cracks and Eqn.(14), we find,

$$ch\frac{\partial(\hat{\sigma}_{11} + \hat{\sigma}_{22})}{\partial x_1} = ch\sum_{N=1}^{\infty} A_N \left(\frac{N}{2} - 1\right) r^{(\frac{N}{2}-2)} \cos(\frac{N}{2} - 2)\phi = \frac{M_1 p}{\Delta}, \tag{22}$$

$$ch\frac{\partial(\hat{\sigma}_{11} + \hat{\sigma}_{22})}{\partial x_2} = ch\sum_{N=1}^{\infty} A_N \left(\frac{N}{2} - 1\right) r^{(\frac{N}{2}-2)} \sin(\frac{N}{2} - 2)\phi = \frac{M_2 p}{\Delta}, \tag{23}$$

where $r$ and $\phi$ are the polar coordinates defined at the crack tip and $A_N$ are constants. Here, $A_1$ is proportional to the stress intensity factor $K_I$ ($A_1 = 2K_I/\sqrt{2\pi}$) and $A_2, ..., A_N$ denote the constant coefficients of the higher order terms. It should be noted that the term corresponding to $N = 2$ in Eqns.(22) and (23) identically vanish. This implies that the constant stress term in $\hat{\sigma}_{11}$ of the Williams' expansion does not contribute to the formation of the fringes in CGS. This feature, could be an advantage if a single parameter fit of the experimental data is sought.

A $K$-dominant crack tip field can now be defined as the one in which the contribution from $N \geq 2$ terms is negligible when compared to the first term. Thus, when a $K$-dominant field exists near the crack tip, Eqns.(22) and (23) reduce to,

$$ch\frac{K_I}{\sqrt{2\pi}} r^{-3/2} \cos(3\phi/2) + O(r^{-1/2}) = \frac{M_1 p}{\Delta}, \tag{24}$$

$$ch\frac{K_I}{\sqrt{2\pi}} r^{-3/2} \sin(3\phi/2) + O(r^{-1/2}) = \frac{M_2 p}{\Delta}, \tag{25}$$

where the negative sign has been absorbed in to fringe orders $M_\alpha$. Now let us define two functions $Y^{(1)}$ and $Y^{(2)}$ as follows:

$$Y^{(1)}(r, \phi) = \left(\frac{M_1 p}{\Delta}\right) \frac{\sqrt{2\pi}}{ch} \frac{r^{3/2}}{\cos(3\phi/2)}, \tag{26}$$

$$Y^{(2)}(r,\phi) = \left(\frac{M_2 p}{\Delta}\right)\frac{\sqrt{2\pi}}{ch}\frac{r^{3/2}}{\sin(3\phi/2)}. \quad (27)$$

It is apparent from the above two relations that when a $K$-dominant field adequately describes crack tip deformations, then $Y^{(\alpha)}$ ($\alpha = 1,2$) is identically equal to the mode-I stress intensity factor $K_I$. To measure $Y^{(\alpha)}$ from fringe patterns, the pictures are digitized and fringe order ($M_\alpha$) and radial distance ($r$) along different directions ($\phi$) around the crack tip are tabulated. Functions $Y^{(\alpha)}$ are plotted against normalized radial distance ($r/h$) in Figs.(7). The predicted value of $K_I$ based on the applied load measurement is indicated as $K_I^{2D}$ [16]. Interestingly, a $K$-dominant field seems to exist near the crack tip in this specimen geometry ($a/w = 0.2$). This is reflected by the constant value of $Y^{(\alpha)}$ which is within about 10% of the predicted value in the range $0.5 < r/h < 1.25$. When $(r/h) < 0.5$, however, the data seem to under estimate the value of $K_I^{2D}$ by more than the typical experimental errors that one would anticipate. One can attribute this behavior to the three dimensional deformations which dominate the immediate vicinity of the crack tip [14].

Existence of a significantly large region of $K$-dominance is not automatic in all fracture specimen geometries. In Fig.(8a), crack tip fringe pattern $\frac{\partial(\hat{\sigma}_{11}+\hat{\sigma}_{22})}{\partial x_1}$ for a specimen geometry with $a/w = 0.32$ is shown. The corresponding $Y^{(1)}$ *vs* $r/h$ plot is shown in Fig.(8b). It is clearly evident from the plot that, even beyond the so-called 3-D zone ($0 < r/h < 0.5$), $Y^{(1)}$ is not a constant and hence $K$-dominance assumption is inadequate for interpreting fringe patterns in this situation. Under such circumstances, the contributions of higher order terms to the crack tip field can be accounted for using Williams' asymptotic field [Eqns. 23,24]. An over deterministic least square analysis is performed using the digitized data to delineate the higher order contributions from the $K$-dominant contributions. A systematic approach of determining the appropriate number of higher order terms to be used in the data processing is discussed in detail in Ref.[17]. A three term ($A_1$, $A_3$, $A_4$) expansion field, in this case, seems to fit the experimental data reasonably well (see, Fig.8a - broken line). Besides, the value of $K_I$ measured is in good agreement with the predicted value $K_I^{2D}$ based on the boundary load measurement.

Applicability of CGS to opaque solids is demonstrated by using the technique in *reflection* mode [Fig.(2)] to map surface deformations in single edge notch, three point bend specimen made of PMMA (plate thickness of 11.7 mm). Commercially available PMMA sheets have about 5-7% of reflectance per surface. This feature is made use of in reflection CGS experiments presented here. The crack tip region is illuminated by a collimated laser beam using a beam splitter and the rear surface reflections are eliminated by painting the surface by flat white paint. Thus, the notch tip interference patterns in this case are produced entirely due to the nonuniform out-of-plane surface displacements. The fringe patterns observed in reflection CGS are shown in Fig.(9). As previously described, they represent contours of constant surface gradients $\frac{\partial u_3}{\partial x_\alpha}$ where $u_3$ is the out-of-plane displacement component. The sensitivity of measurement is approximately 0.0125 degrees/fringe - twice that of transmission CGS for the same values of experimental parameters ($p$ and $\Delta$). These fringe patterns can be interpreted, in a manner similar to transmission CGS patterns, using Eqn.(21) and the Williams expansion field for $(\hat{\sigma}_{11} + \hat{\sigma}_{22})$ [see Ref.15 for details].

*(b) Dynamic Crack Growth Experiments*

Dynamic crack propagation experiments are conducted using fracture specimens made of PMMA sheets. The specimen geometry is similar to the one shown Fig.5. A 0.75 mm thick stater notch is cut in these specimens. For reflection CGS, the specimen is made specularly reflective by depositing a layer of aluminum using vacuum deposition process whereas no special preparation is required for transmission specimens.

The specimens are subjected to dynamic loading in a Dynatup 8100A drop-weight tower with impact velocities in the range of 2-5 m/sec. The freely falling weight impacts and loads the specimen dynamically to the point of crack initiation followed by rapid crack propagation. The experimental configuration provides mode-I loading conditions. The interference patterns due to dynamic crack tip deformation fields are

recorded using high speed photography. A cavity-dumped Argon-Ion laser pulsing with a repetition rate of 7-10 $\mu s$ and 50 $ns$ pulse width is used as the strobe light source. The region of interrogation in these experiments is approximately 50 mm diameter region around the crack tip. The event is recorded using an air turbine driven, rotating mirror type, continuous access, streak camera. The falling weight when contacts the specimen, triggers the light source to produce light pulses at the above said rate for a duration of less than or equal to the pre-set period of the rotating mirror to avoid over writing or overlapping of images on the film track.

The time sequence of a typical transmission and reflection CGS interference patterns are shown in Fig.11 and Fig.12, respectively. They represent the deformation field $ch\frac{\partial(\hat{\sigma}_{11}+\hat{\sigma}_{22})}{\partial x_1}$ and $\frac{\partial u_3}{\partial x_1}$ near the propagating crack, respectively. The sensitivity of measurements are same the ones used in the static experiments. The crack velocity in both the cases is constant and is approximately 300 m/s.

Freund and Clifton (1974) have shown that the stress field with reference to a Cartesian coordinate system moving with a smoothly propagating crack tip, for all plane elastodynamic solutions under mode-I conditions, can be asymptotically described by the square-root singular expression:

$$\hat{\sigma}_{\alpha\beta}(r,\phi) = \frac{K_I^d(t)}{\sqrt{2\pi r}}\Sigma_{\alpha\beta}^I(\phi,\dot{a}) + O(1), \text{ as } r \to 0. \tag{28}$$

Here $(r,\phi)$ is a polar coordinate system travelling with the crack-tip, $\Sigma_{\alpha\beta}^I$ are known universal functions of $\phi$ and $\dot{a}$ is the crack velocity (with respect to some fixed coordinate frame). Indeed, $K_I^d(t)$, the so-called dynamic stress-intensity factor in Mode-I, is the only factor which is dependent on the specific geometry and loading conditions. Any finite region around the crack tip where the above *asymptotic* field dominates (to within some acceptable error) will be referred to as a $K_I^d$-dominant region.

The transmission CGS fringe patterns are digitized for analysis to get fringe order $(M_1)$ and location $(r,\phi)$ with respect to the crack-tip at each instant in time. If we now assume that the crack-tip fields are $K_I^d$-dominant, we find, using Eqn. (28) in the fringe relations (14) that:

$$ch\mathcal{D}(\dot{a})\frac{K_I^d}{\sqrt{2\pi}}r_l^{-3/2}\cos(3\phi_l/2) + o(r^{-3/2}) = \frac{M_1 p}{\Delta}. \tag{29}$$

In the above,

$$\mathcal{D}(\dot{a}) = \frac{(1+\alpha_s^2)(\alpha_l^2-\alpha_s^2)}{4\alpha_l\alpha_s-(1+\alpha_s^2)^2}, \qquad \alpha_{l:s} = \left\{1-\left(\frac{\dot{a}}{c_{l:s}}\right)^2\right\}^{1/2},$$

$$r_l = r\cos\phi\{1+\alpha_l\tan^2\phi\}, \qquad \phi_l = \tan^{-1}\{\alpha_l\tan\phi\},$$

and $c_l$ and $c_s$ are the longitudinal and shear wave speeds of the material, respectively. Now, one can define a function $Y_1^d(r,\phi)$ as follows:

$$Y_1^d(r,\phi) = \left(\frac{M_1 p}{\Delta}\right)\frac{\sqrt{2\pi}}{ch\mathcal{D}(\dot{a})}\frac{r_l^{3/2}}{\cos(3\phi_l/2)}, \tag{30}$$

It is apparent from the above and Eqn. (29) that in regions where $K_I^d$-dominance holds, $Y_1^d$ would be a constant equal to the instantaneous dynamic stress-intensity factor $K_I^d$ to within experimental error.

Figure (13) shows the plot of $Y_1^d$ against $(r/h)$ for a specimen PD-11 at a time instant a few microseconds after crack initiation $(a/w{=}0.23)$. Apparently, there seems to be *no* region around the crack tip over which the function $Y_1^d$ is constant. Indeed the spread in $Y_1^d$ values from different locations is as much as 400%. Obviously, extraction of the dynamic stress intensity factor value cannot be based here on a simplistic assumption of near tip $K_I^d$-dominance. On the other hand, however, under static conditions, for an $(a/w)$ ratio of 0.2 we do seem to have a significant region $(0.5 < r/h < 1.25)$ of $K_I$-dominance. This suggests that

*even though a specimen might exhibit a sizeable region of $K_I$-dominance under* static *loading conditions, there might be no corresponding region of $K_I^d$-dominance under* dynamic *conditions.*

Thus, $K_I^d$-dominance assumption does not appear to hold for a dynamically propagating crack at least for times immediately after crack initiation. The initiation of a crack from a pre-cut notch is expected to be a *highly transient* event, and this could be one source of the observed lack of $K_I^d$-dominance in the experiments. If so, could a $K_I^d$-dominant region develop around the propagating crack tip once the initiation transients have attenuated? In Fig.(13), $Y_1^d$ *vs* $r/h$ for a later time slice, indicates that continuing higher order transient effects and possible boundary interaction with the crack tip preclude the establishment of a truly $K_I^d$-dominant region for this specimen/loading configuration. In order to make sure that the above phenomenon is not due to the rate dependence of the stress-optic constant, the data from the reflection tests are analyzed in a manner similar to the one described above. Detailed discussion of the same can be found in Ref.[18]. A plot of the reflection counterpart of $Y_1^d$ namely, $Z_1^d$ is plotted is plotted against $r/h$ in Fig.(14) which again shows a similar lack of $K_I^d$-dominance as seen in transmission experiments.

In the absence of $K_I^d$-dominance, the use of steady state higher-order terms is commonly employed when the method of photoelasticity [19] is used. However, recently a transient, higher-order stress field for propagating cracks has been presented by Freund and Rosakis [20] wherein one need not have to assume a steady state crack propagation. Based on this analysis, for transmission CGS fringe patterns, the following expression can be written for a constant velocity crack propagation:

$$\begin{aligned} Y_I^d = \quad & K_I^d + \left\{\beta_2 \frac{\cos(\phi_l/2)}{\cos(3\phi_l/2)} + \beta_3 \frac{\cos(5\phi_l/2)}{\cos(3\phi_l/2)}\right\} r_l + \left\{\beta_4 \frac{1}{\cos(3\phi_l/2)}\right\} r_l^{3/2} + \\ & \left\{\beta_5 \frac{\cos(\phi_l/2)}{\cos(3\phi_l/2)} + \beta_6 + \beta_7 \frac{\cos(7\phi_l/2)}{\cos(3\phi_l/2)}\right\} r_l^2 + \left\{\beta_8 \frac{\cos(\phi_l)}{\cos(3\phi_l/2)}\right\} r_l^{5/2} + o(r^3), \end{aligned} \tag{31}$$

where $\beta_2$-$\beta_8$ are constants to be determined. Under $K_I^d$-dominance, $Y_1^d$ will be a constant and equal to the instantaneous stress intensity factor $K_I^d$.

A least-squares procedure analogous to the one used in the static analysis is used to fit the right hand side of the above equation to the digitized experimental data ($Y_1^d$) in the region $r/h > 0.5$. Figure (15) shows the results for one particular time instant during crack propagation in specimen PD-11. It shows good agreement between the reconstructed fringe pattern using the transient analysis (dotted lines) and the experimentally obtained fringes. This conclusively shows that *the observed lack of $K_I^d$-dominance in the two-dimensional region outside the near-tip three-dimensional zone is due to the important contribution of higher-order terms to the total stress and deformation fields around the crack-tip.*

*(c) Crack Growth Along Bimaterial Interfaces*

Applicability of CGS to the study of the failure of material interfaces is demonstrated by using the method for mapping crack tip deformation fields near propagating bimaterial interface cracks. Bimaterial specimens are subjected to symmetric three point bending [Fig.(16a)]. The specimens are made from equal thickness sheets (thickness $h$=9 mm) of commercially available PMMA (material-1) and Al 6061-T6 (material-2). The two halves of the specimen are machined to ensure square edges and the bond between the two materials is created using a commercially available[4] methyl methacrylate monomer (MMA) (compound-A) which polymerizes at room temperature when mixed with a catalyst (compound-B). This results in a bond material with stiffness characteristics similar to that of material-1 (see, Ref.[21] for details). The thickness of the bond so obtained is approximately 100 $\mu$m. The specimen has a starter edge notch of length 25 mm cut along the interface with a band saw of thickness 0.75 mm. The experiments are conducted using transmission CGS. Naturally, this allows us to measure crack tip deformations only in the transparent (PMMA) half of the specimen. Under displacement controlled loading, a crack initiates

[4]commercial name: Weldon-10 A&B, manufactured by IPS Corporation, Gardena, CA.

at the pre-cut notch tip and propagates quasi-statically along the interface. The interference fringes that represent the deformation $ch\frac{\partial(\hat{\sigma}_{11}+\hat{\sigma}_{22})}{\partial x_1}$ near the crack tip in PMMA.

In Fig.(16b) interference fringes from the bimaterial specimen PAS-8 for $a/w$=0.21 is shown. The resolution of measurement is 0.025°/fringe. These interference patterns are analyzed using two dimensional, singular, interfacial crack tip stress fields given by Rice, Suo and Wang [22]. For the deformation field under consideration, $K$-dominant assumption in material-1 leads to,

$$ch\frac{\partial(\hat{\sigma}_{11}+\hat{\sigma}_{22})}{\partial x_1} = \frac{chr^{-3/2}e^{\varepsilon(\phi-\pi)}}{\sqrt{2\pi}\cosh(\pi\varepsilon)}\left[-Q_1\cos(\frac{3\phi}{2}+\varepsilon\ln\frac{r}{a})-2\varepsilon Q_1\sin(\frac{3\phi}{2}+\varepsilon\ln\frac{r}{a})\right.$$
$$\left.+Q_2\sin(\frac{3\phi}{2}+\varepsilon\ln\frac{r}{a})-2\varepsilon Q_2\cos(\frac{3\phi}{2}+\varepsilon\ln\frac{r}{a})\right]=\frac{M_1 p}{\Delta}, \quad (32)$$

where $r,\phi$ are the crack tip polar coordinates, $Q_1=|K|\cos\psi$, $Q_2=|K|\sin\psi$ and $K$ $(=K_1+iK_2)$ is the so-called complex stress intensity factor. The material mismatch parameter $\varepsilon$ is given by,

$$\varepsilon=\frac{1}{2\pi}\ln\left[\left(\frac{\kappa_1}{\mu_1}+\frac{1}{\mu_2}\right)/\left(\frac{\kappa_2}{\mu_2}+\frac{1}{\mu_1}\right)\right],$$

where $\kappa_i=\frac{3-\nu_i}{1+\nu_i}$ for plane stress and $\nu_i$ and $\mu_i$ $(i$=1,2) are the Poisson's ratio and shear modulus for material-1 and material-2, respectively. The phase angle $\psi$ using crack length $a$ as the length scale is,

$$\psi(a)=\tan^{-1}[Im(Ka^{i\varepsilon})/Re(Ka^{i\varepsilon})]. \quad (33)$$

In Eqn.(32) note that although remote loading is symmetric, the crack tip field is has both symmetric and antisymmetric contributions due to the mismatch in elastic properties between the two materials. The fringe patterns are digitized to obtain fringe order $(M_1)$ and fringe location $(r,\phi)$ in the crack tip region. The experimental data can be analyzed using the above described (Eqn.(32)) field only if the measured field is well approximated by plane stress conditions. In a three dimensional elastostatic finite element analysis of a tensile bimaterial strip with a Griffith crack [23], near an interface crack, three dimensional deformations seem to occur all along the interface ahead of the crack tip ($0^o\leq\phi\leq 45^o$). However, in the region $45^o\leq\phi\leq 150^o$, three dimensional deformations seem to decay to a 2-D field beyond $r/h\approx$0.5. This allows one to use Eqn.(32) for interpreting the experimental data in the region behind the crack tip ($90^o\leq\phi\leq 150^o$). A least square data analysis is performed to determine $Q_1$ and $Q_2$ from the experimental data. Thus, $|K|^{exp}$ $(=\sqrt{Q_1^2+Q_2^2})$ and $\tan^{-1}(K_2/K_1)$ are calculated and are compared with those obtained from plane stress finite element calculations performed, on an identical specimen geometry and material mismatch $\varepsilon$, by O'Dowd and Shih [24]. The measured and predicted values $|K|$ are in reasonably good agreement. A detailed discussion of the same is available in Ref.[21].

## Conclusions

A real time optical interferometry called Coherent Gradient Sensing is developed for fracture mechanics applications in general and dynamic fracture investigations in particular. The method being full field and capable of working well in both transmission and reflection modes, provides an effective alternative to other optical methods used for crack tip field investigations. The first order diffraction analysis indicates that the interference patterns measured by the method are related to the local direction cosines of the propagating wave front. These in turn are related to the crack tip stress and deformation gradients.

Several examples demonstrating the applicability of CGS to study quasi-static and dynamic fracture in homogeneous and bimaterial solids are presented. Analysis of the fringes suggests a general lack of $K$-dominance in the specimen geometries investigated. The interpretation of the full field data using expansion fields seem to suggest that it is necessary to account for geometric and/or transient effects in analyzing the experimental data in two dimensional regions.

## References


1. C.W. Smith and A.S. Kobayashi, *Handbook of Experimental Mechanics*, A.S. Kobayashi (Ed.), (1987), Prentice-Hall, pp 891-956.

2. R. Chona, G.R. Irwin and R.J. Sanford, *ASTM STP 791*, 1, (1983), pp 3-13.

3. H.W. Liu and J.S. Ke, *Experimental Techniques in Fracture Mechanics -2*, SESA Monography, A.S. Kobayashi (Ed.), 1975, pp 59-87.

4. F.P. Chiang and T.V. Hareesh, *Int. J. Fracture*, 36, (1988), pp 243-257.

5. J. Beinert and J.F. Kalthoff, *Mechanics of Fracture*, Vol. VII, G.C. Sih, (Ed.), Sijthoff and Noordhoff, (1981), pp 281-330.

6. A.J. Rosakis and L.B. Freund, *J. Eng. Mater. Tech.*, 104, (1982), pp 115-120.

7. C.W. Smith, D. Post, G. Hiatt and G. Nicoletto, Exp. Mech., 23(1), (1983), pp 15-20.

8. T.D. Dudderar and R. O'Regan, *Exp. Mech*, 11(2), (1971), pp 49-56.

9. A.T. Zehnder and A.J. Rosakis, *J. Applied Mech.*, 57, (1990), pp 618-626.

10. A.A. Wells and D. Post, *Proc. Soc. Exp. Stress Analysis*, 16, (1958), pp 69-92.

11. T. Kobayashi and J.W. Dally, *Crack Arrest Methodology*, G.T. Hahn and M.F. Kanninen (Eds.), *ASTM STP 711*, (1980), pp 189-239.

12. K. Ravi-Chandar and W.G. Knauss, *Int. J. Fract.*, 20, (1982), pp 204-222.

13. H.V. Tippur, S. Krishnaswamy and A.J. Rosakis, *Int. J. Fract.*, 48, (1991), pp 193-204.

14. A.J. Rosakis and K. Ravi-Chandar, *Int. J. Solids and Structures*, 21(9), (1985), pp 977-994.

15. M.L. Williams, *J. Applied Mechanics*, 24, (1959), pp 109-114.

16. D.P. Rooke and D.J. Cartwright, *Compendium of Stress Intensity Factors*, Her Majesty's Office, (1975).

17. H.V. Tippur, S. Krishnaswamy and A.J. Rosakis, Caltech Report SM89-11, to appear in *Int. J. Fract.*, (1991).

18. S. Krishnaswamy, H.V. Tippur and A.J. Rosakis, Caltech Report SM90-1, to appear in *J. Mech. Phys. Solids*, (1991).

19. J.W. Dally, W.L. Fourney and G.R. Irwin, Int. J. Fract., 27, (1985) pp 159-168.

20. L.B. Freund and A.J. Rosakis, 11th National Congress of Applied Mechanics, Tuscon, AZ, 1990.

21. H.V. Tippur and A.J. Rosakis, Caltech Report SM 90-18, to appear in *Exp. Mech.*, (1992).

22. J.R. Rice, Z. Suo and J.S. Wang, *Metal-Ceramic Interfaces*, Acta-Scripta Met. Proc. Series, 4, (1990), pp 269-294.

23. T. Nakamura, 11th National Congress of Applied Mechanics, Tuscon, AZ, 1990.

24. N.P. O'Dowd and C.F. Shih, Private Communications, April, 1990.

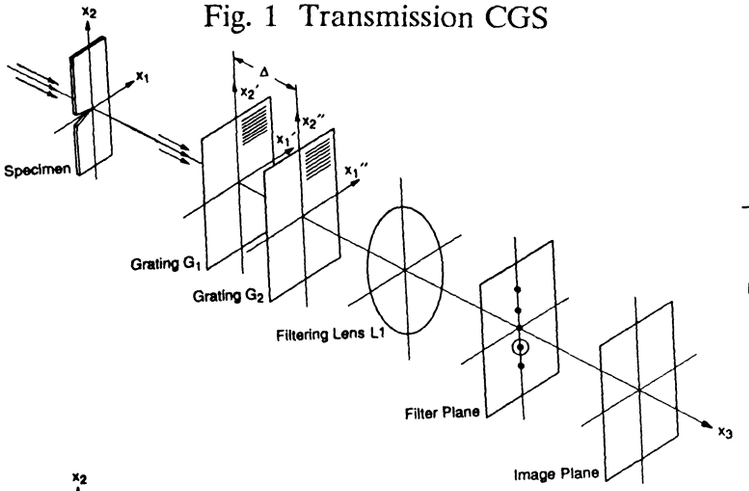


Fig. 1 Transmission CGS

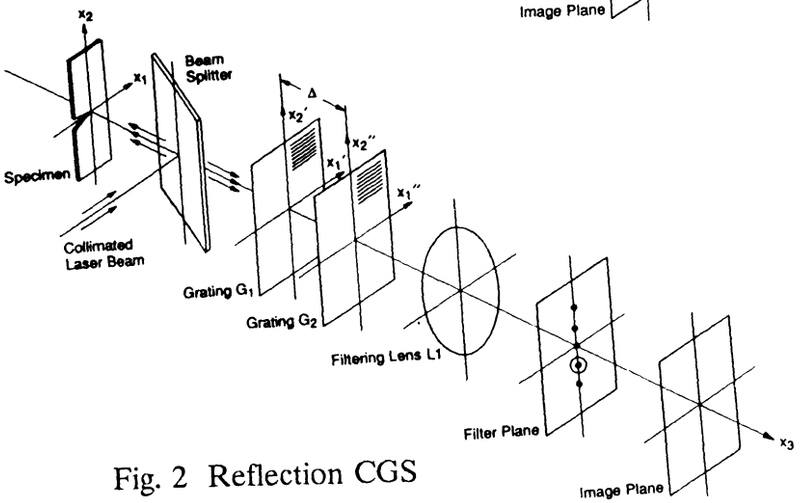


Fig. 2 Reflection CGS

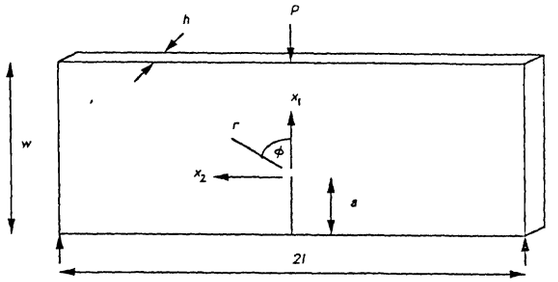


Fig. 5 Fracture specimen

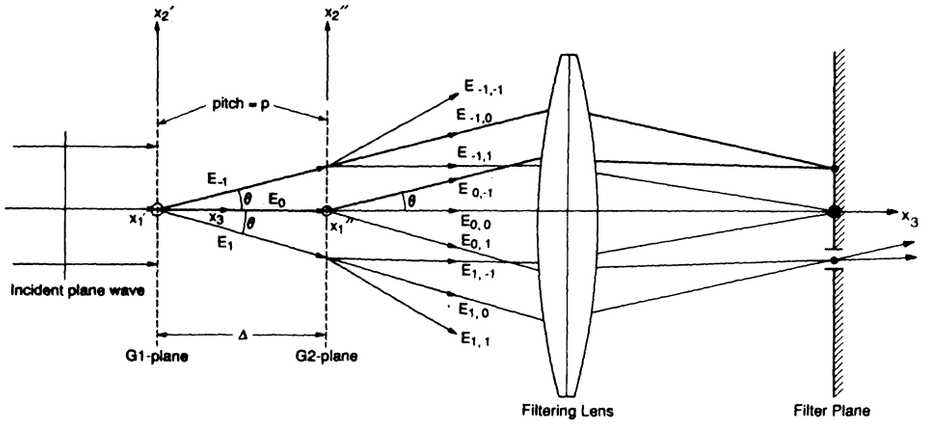


Fig. 3 Working principle

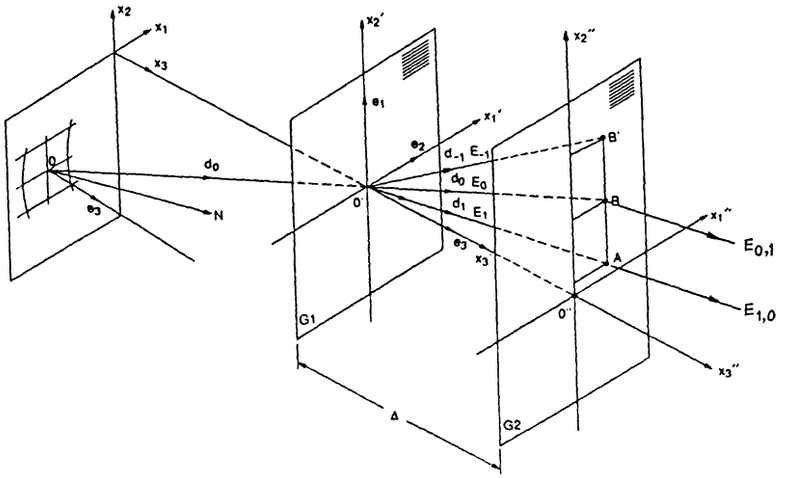


Fig. 4 Diffraction of a generic ray

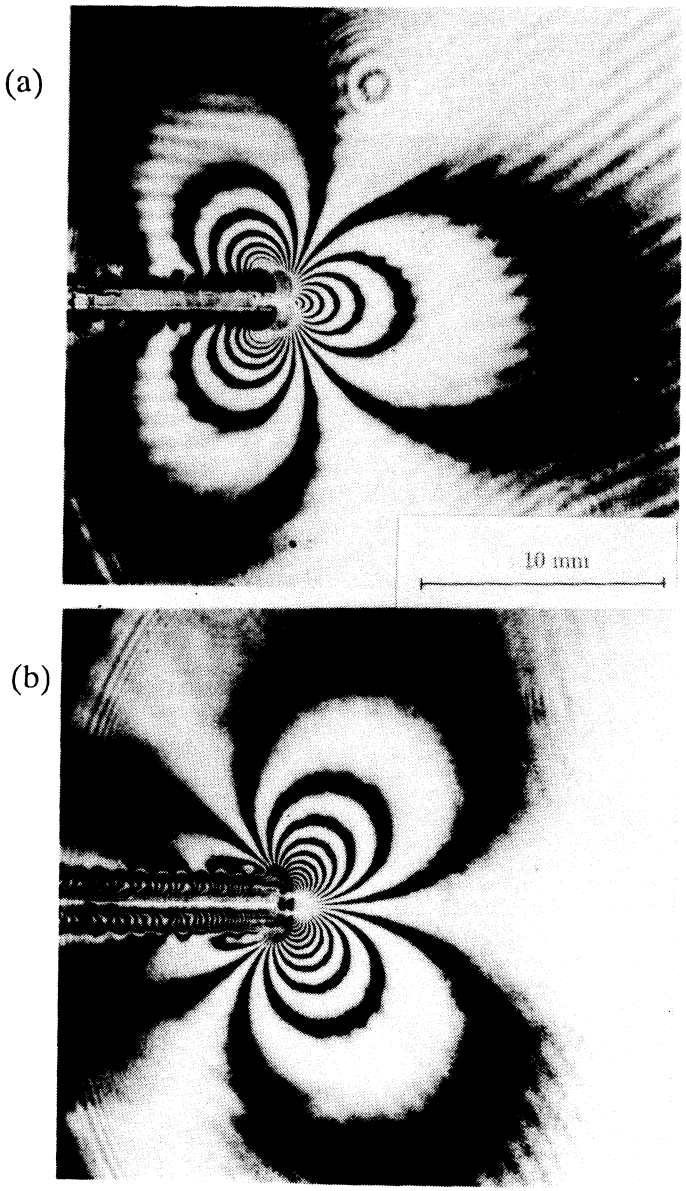


Fig.6 Contour maps of $\partial(\sigma_{11}+\sigma_{22})/\partial x_1$ and $\partial(\sigma_{11}+\sigma_{22})/\partial x_2$ from transmission CGS

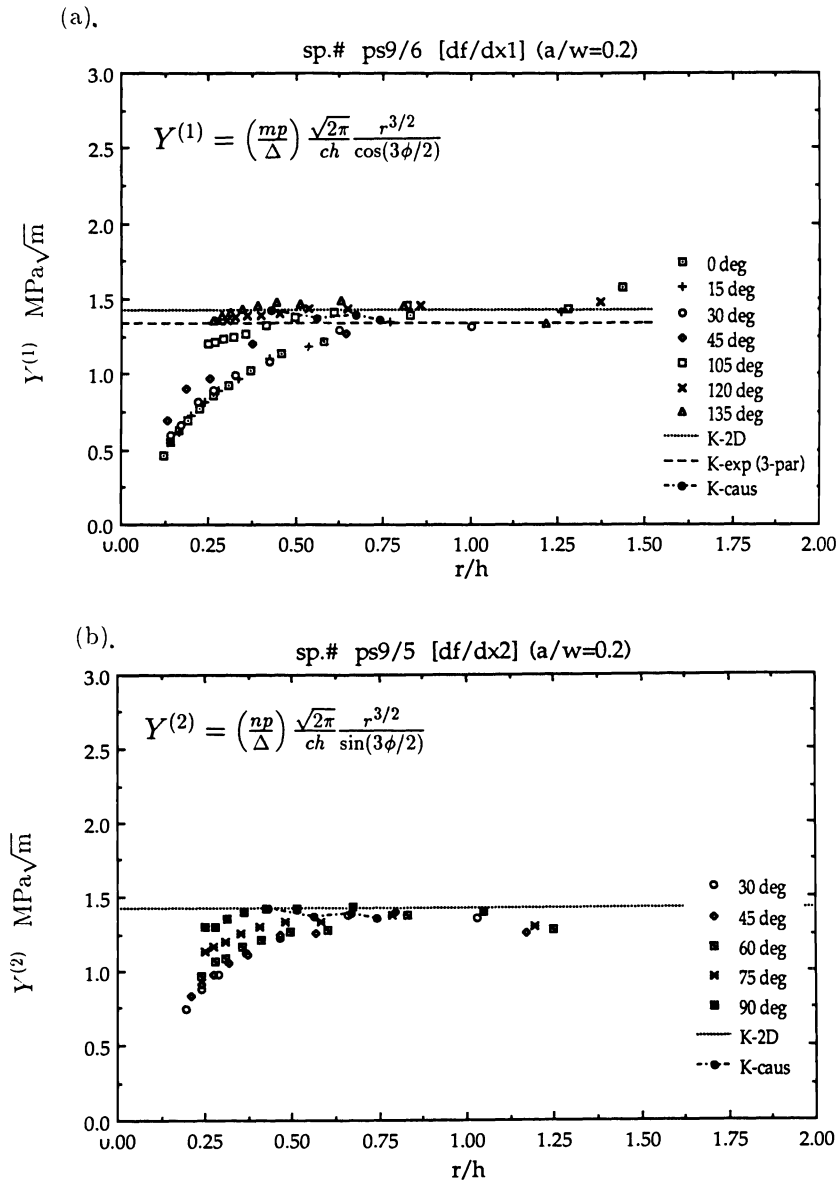


Fig. 7 Radial plots of experimental stress intensity factors measured from fig. 6(a) and (b)

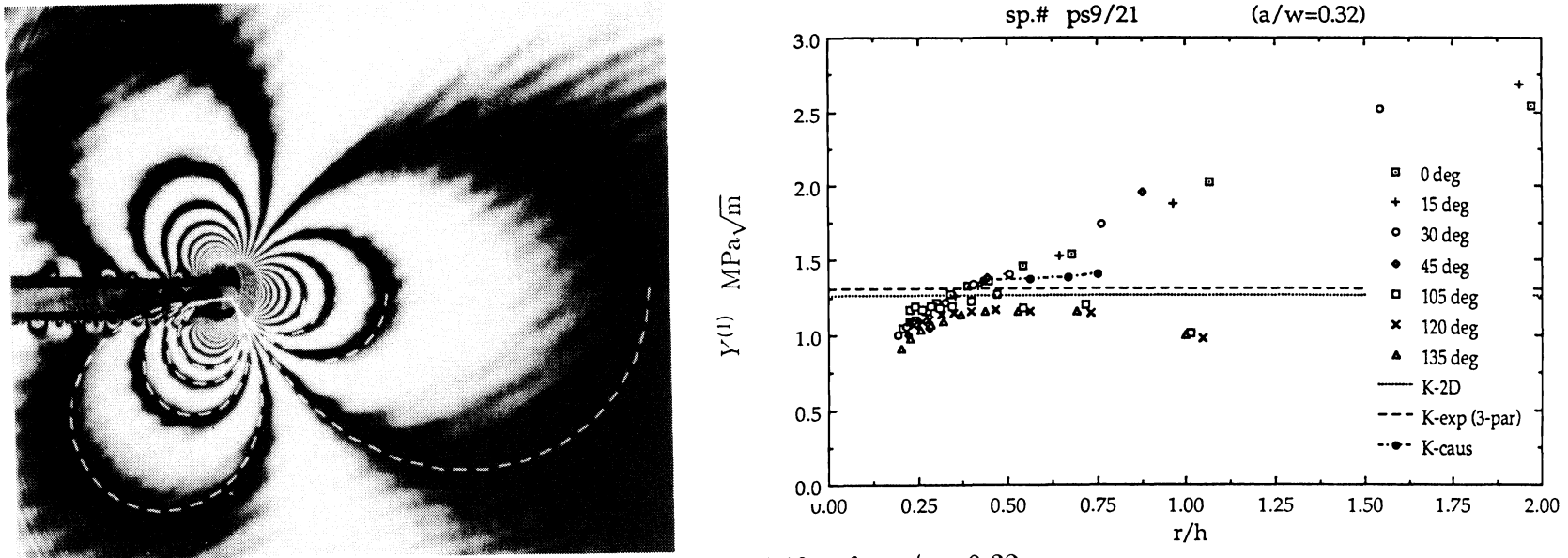


Fig.8 (a) Contours of $\partial(\sigma_{11}+\sigma_{22})/\partial x_1$ for $a/w$=0.32
(b) Radial plot of experimental SIF for fringes shown in Fig.8a

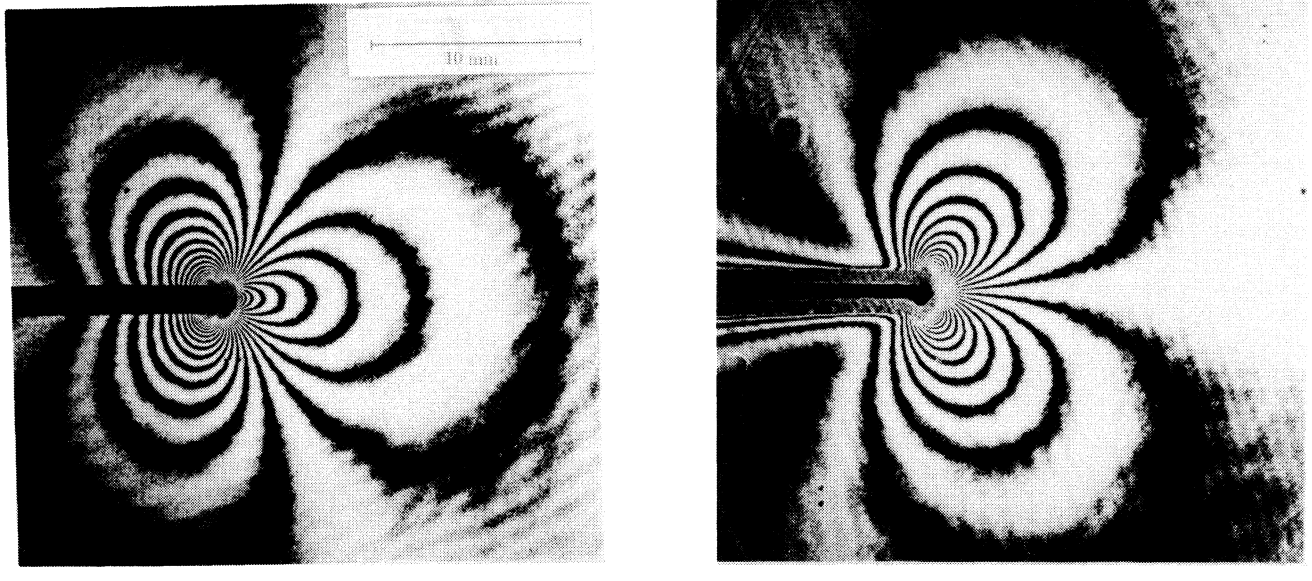

Fig.9 Contour maps of $\partial u_3/\partial x_1$ and $\partial u_3/\partial x_2$
from reflection CGS

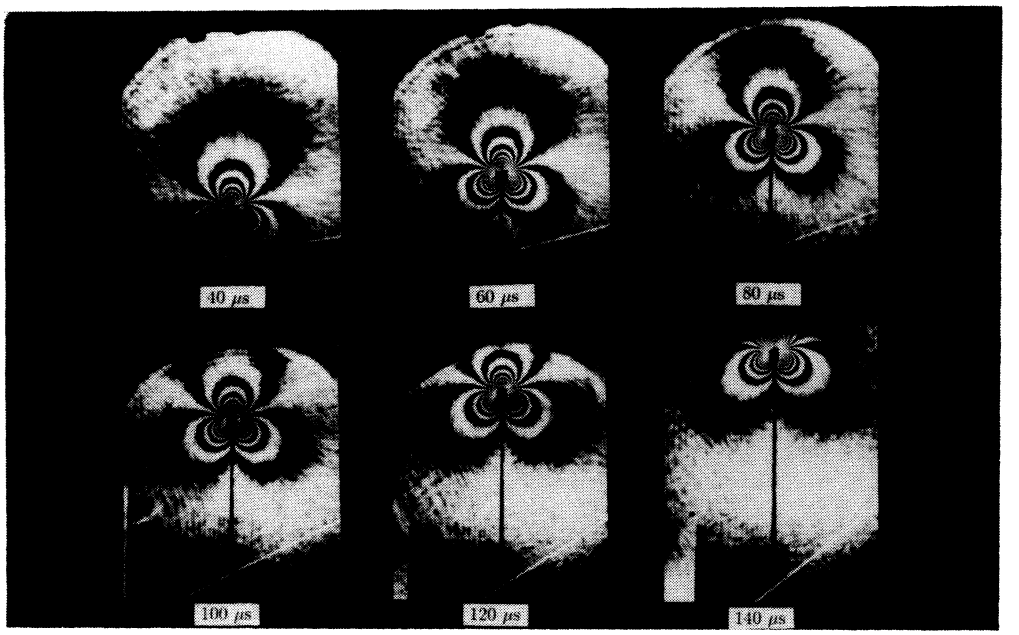


Fig. 10 Time sequence of $\partial(\sigma_{11}+\sigma_{22})/\partial x_1$ fringes near a dynamically growing crack in PMMA obtained using transmission CGS

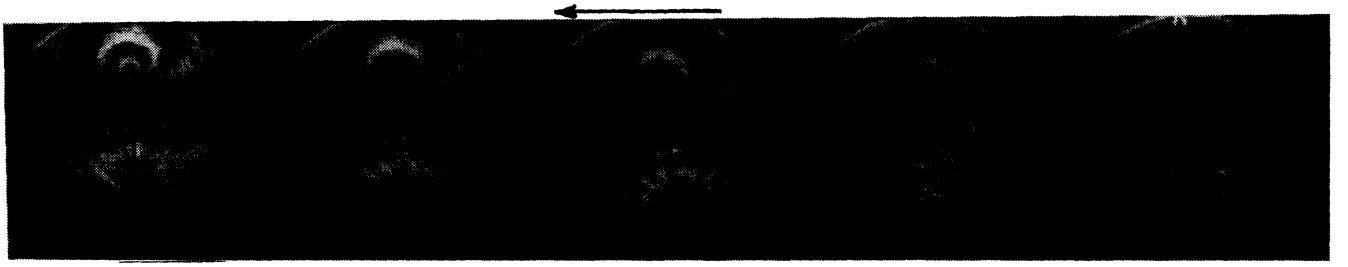

Fig. 11 Time sequence of $\partial u_3/\partial x_1$ fringes near a dynamically growing crack in PMMA obtained using reflection CGS

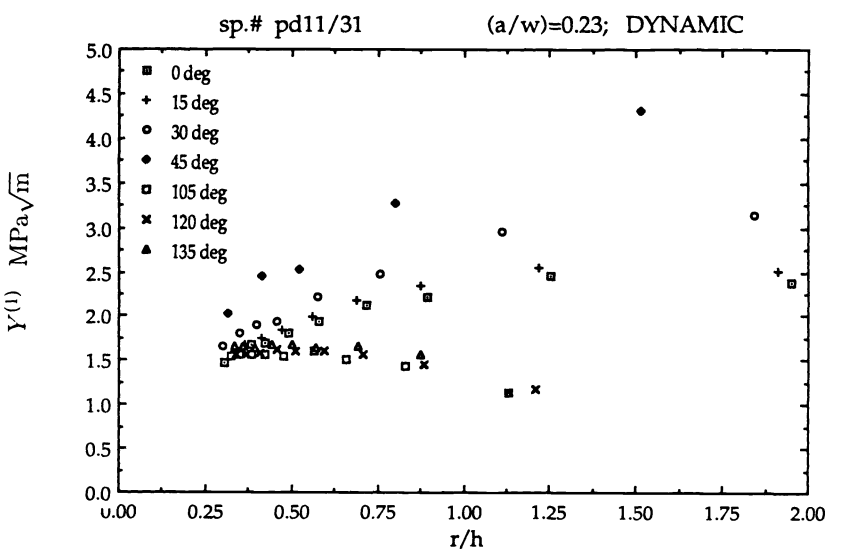


Fig. 12 Radial plat of experimental dynamic SIF for a time instant 20 micro-sec. after initiation

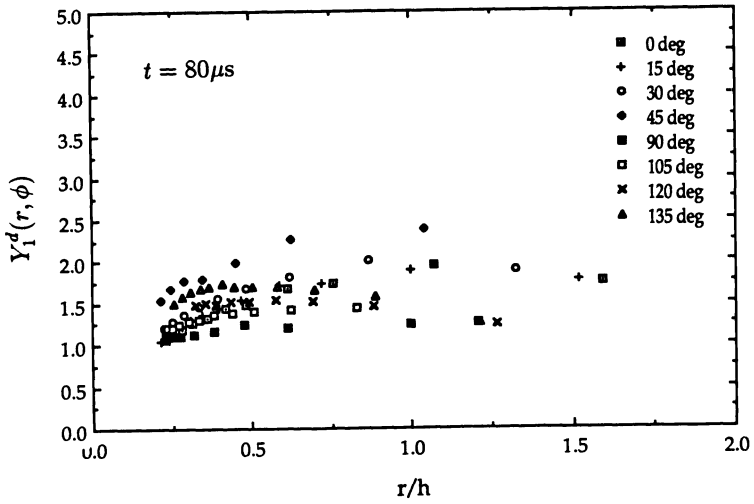


Fig. 13 Radial plot of experimental dynamic SIF $80\mu s$ after crack initiation

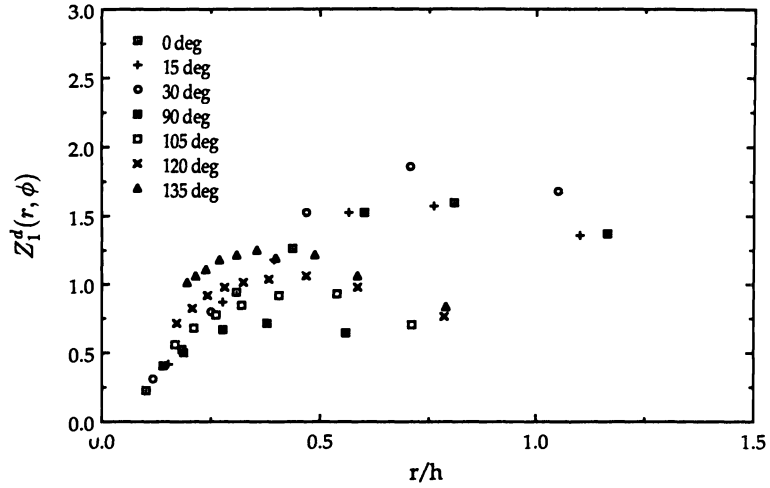


Fig. 14 Radial plot of experimental dynamic SIF from reflection CGS fringes

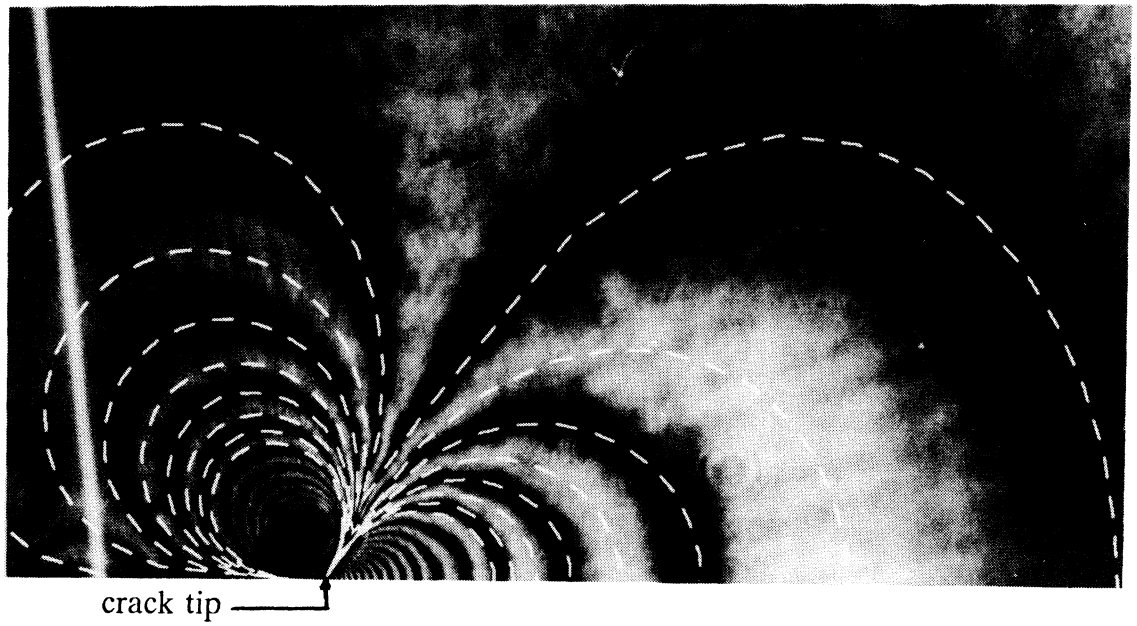


Fig. 15 Synthetic transmission CGS fringes (broken line) obtained from transient expansion field analysis superimposed on actual fringes

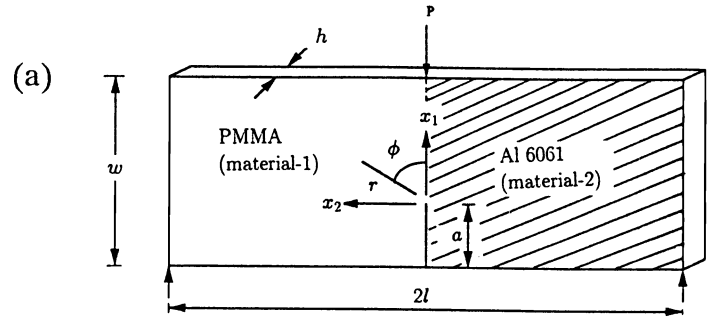


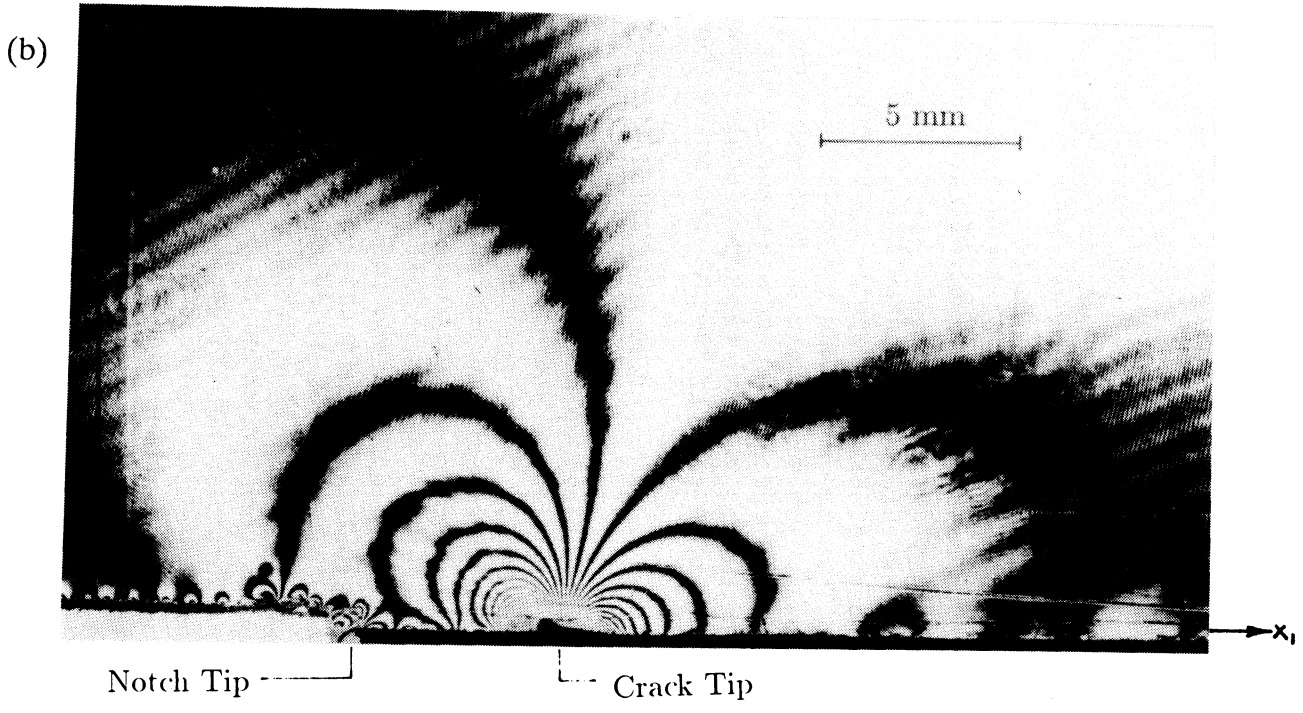


Fig. 16 (a) Bimaterial fracture specimen geometry, (b) Contour maps of crack tip $\partial(\sigma_{11} + \sigma_{22})/\partial x_1$ field in the PMMA half